Stability Transition in Gap Expansion-Driven Interfacial Flow

Dongqi Li,[1,2,3] Zhibing Yang [1,2,*] Amir A. Pahlavan,[4] Renjun Zhang [1,2] Ran Hu,[1,2] and Yi-Feng Chen[1,2,†]

[1]*State Key Laboratory of Water Resources Engineering and Management, Wuhan University,*
Wuhan 430072, People's Republic of China

[2]*Key Laboratory of Rock Mechanics in Hydraulic Structural Engineering of the Ministry of Education, Wuhan University,*
Wuhan 430072, People's Republic of China

[3]*Henan Provincial Key Lab of Hydrosphere and Watershed Water Security, North China University of Water Resources and*
Electric Power, Zhengzhou 450046, People's Republic of China

[4]*Department of Mechanical Engineering and Materials Science, Yale University, New Haven, Connecticut 06511, USA*

We investigate interfacial instability in a lifting Hele-Shaw cell by experiments and theory. We characterize the unexplored transition from stable to unstable patterns under a wide range of controlling parameters. Surprisingly, we find that the perturbation growth rate-based criterion for the onset of instability from linear stability theory is too strict by over 3 orders of magnitude. To reconcile this striking discrepancy, we propose a new criterion based on perturbation amplitude, which is in excellent agreement with the experimental results. We further show that the fingering pattern evolves to produce a hierarchical fluid structure and derive a theoretical equation to predict the fingering evolution.

The displacement of one fluid by another immiscible, less viscous fluid is a ubiquitous process, often featuring interfacial instabilities and forming intriguing patterns [1–5]. This process occurs widely in biological structures, geophysical processes, and industrial applications and can become rather complex when the confining space is undergoing deformation, especially in cell growth [6,7], pulmonary airway closure and reopening [8,9], oil and gas extraction [10,11], and adhesive interlayer debonding [12,13]. Hence, it is of scientific significance and technological importance to understand and control pattern formation in deformation-driven interfacial flows.

Interfacial patterns in the classical Hele-Shaw-type experiments are often studied with a focus on the onset of instability characterized by finger-shaped interface propagation. Many strategies have been proposed to suppress the interface stability, including tilting geometry [14–16], elastic membrane boundary [17–19], time-dependent flow rate [20–22], and time-dependent flow geometry [23]. Of particular interest is the lifting Hele-Shaw setup (where the top plate is lifted with a constant velocity) due to its relevance to applications in adhesion strength problems [12,24–27]. The lifting configuration has been studied for both Newtonian [12,13,24,28–31] and non-Newtonian fluids [25–27,32–35]. For Bingham fluids, the competition of viscous and yield stresses dictates the stability, and an energy-based criterion was recently shown to explain the stability transition [35]. For Newtonian fluids, the interface instability is typically assessed through linear stability analysis by inspecting the perturbation growth rate Λ or perturbation amplitude ζ [14,22,29,36]; for systems with constant Λ, the criterion $\Lambda < 0$ guarantees interfacial stability. It is commonly believed that stable patterns are practically not attainable for Newtonian fluids in lifting Hele-Shaw configurations [35], and, thus, most of the previous studies focus only on characterizing the unstable pattern by analyzing the number of viscous fingers [12,13]. However, Λ can vary with time t and even change sign, which renders the description based on constant Λ invalid. The experimental transition between stable and unstable patterns in lifting Hele-Shaw cells remains unexplored.

In this Letter, we address the stability problem in lifting Hele-Shaw cells through a comprehensive set of carefully controlled experiments [Fig. 1(a)] and theoretical analysis. We experimentally capture the transition from macroscopically stable to unstable interfacial patterns for Newtonian fluids. In contrast to the common belief, macroscopically stable patterns are observed in a wide range of experimental parameters, even when the system has a positive Λ. Through theoretical calculations of spatiotemporal dynamics of Λ and ζ, we elucidate the mechanism of pattern transition. For flow configurations with a time-evolving Λ, the interfacial stability is better characterized by the perturbation amplitude. We further propose a new amplitude-based criterion to predict the onset of instability. Moreover, we provide a simple analytical expression, which accurately predicts the evolution of finger numbers for the unstable patterns. This work lays a solid foundation for controlling interfacial morphologies in a confined geometry which undergoes large deformation or expansion.

We develop an experimental protocol of interface dynamics in a lifting Hele-Shaw cell where the top plate

034003-1
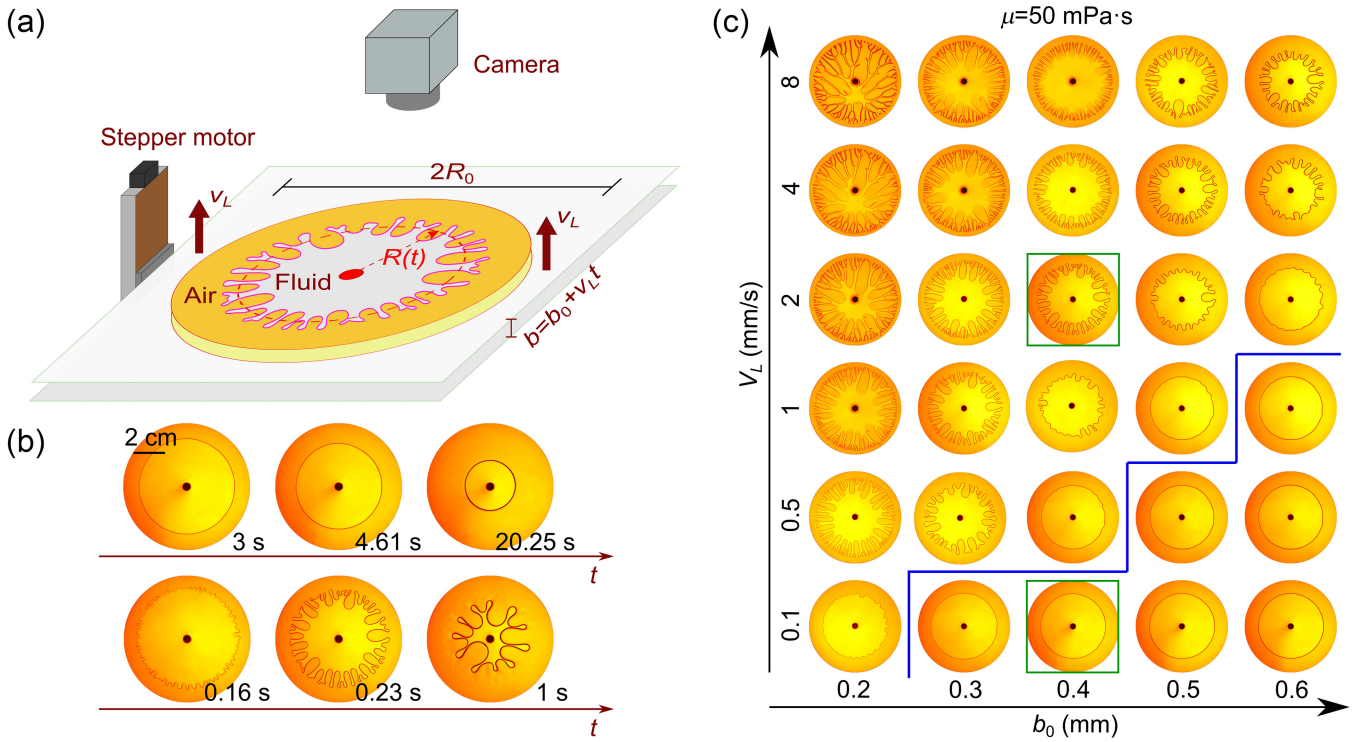
FIG. 1. (a) Schematic of experimental apparatus. (b) Evolution of interface for a stable pattern (upper row) and a typical unstable pattern (bottom row), marked in (c) by green squares. (c) Fluid morphologies for different initial gap b_0 and lift velocity v_L. The blue line separates the stable and unstable patterns. The images are taken at times corresponding to $b/b_0 = 2$ for the stable patterns and the maximal extent of fingering hierarchical structure ($b/b_0 = 1.9 - 2.3$) for the unstable patterns, respectively.

is lifted by a precise stepper motor at a constant velocity [37]. We systematically vary the initial gap b_0 (0.2–0.6 mm), the lift velocity v_L (0.1–8 mm/s), the fluid viscosity μ (50, 100, and 200 mPa·s), and the flow cell size R_0 (25, 30, and 40 mm). Silicone oil (density $\rho =$ 0.963 g/cm^3 and interfacial tension $\sigma = 21$ mN/m with air) is used as the fluid between the gap. The static contact angle of the fluid on the quartz plates tested by a drop shape analyzer (Krüss, DSA25) approaches 0°.

We first establish an experimental pattern diagram (Fig. 1) in the phase space of b_0 and v_L. Additional results under other experimental parameters are presented in [37]. The stable patterns are characterized by nearly circular interface during lifting. In the unstable patterns, a variety of features emerge, ranging from wiggly interfaces to prominent fingering and to treelike fluid structures. The interface in the unstable case experiences at early times a finger growth stage and at late times a decay stage due to considerable stretch of fluid in the gap direction [Fig. 1(b)]. We mainly focus on the first stage in this work. Generally, unstable patterns emerge under high lift velocities, small initial gaps, and high fluid viscosities. In this circumstance, the interface perturbations with large growth rates develop into viscous fingers of air, extending in the radial direction, leading to increasing interface perimeter length L_P. In contrast, for the stable patterns the amplitude of interface

perturbations does not grow into macroscopically observable sizes, and the evolution of perimeter length coincides with the circumference of a shrinking circle; i.e., L_P decreases with time as $L_P = 2\pi R_0[b_0/b(t)]^{1/2}$ according to fluid mass conservation, $R(t)^2 b(t) = R_0^2 b_0$, where $R(t)$ is the equivalent interface radius (Fig. S1 [37]).

The transition between stable and unstable patterns is evident. Based on visual inspection, the boundary between the two regimes is delineated [Fig. 1(c)]. For example, when $b_0 = 0.5$ mm, the interface shifts from a smooth circle to noticeable wiggles as v_L increases from 0.5 to 1.0 mm/s. The perimeter length and interfacial curvature are further used as quantitative metrics of instability. For convenience, we define the normalized perimeter length $\Gamma(t) = L_P(t)/2\pi R(t)$ and the normalized interfacial curvature $\kappa^*(t) = \kappa(t)R(t)$, where the interfacial curvature $\kappa(t)$ is obtained by using an image-based algorithm [11]. Undoubtedly, Γ and $\kappa^*(t)$ being 1 at all times means an absolutely stable interface. Unless otherwise specified, $\kappa^*(t)$ is the minimum of curvature along the interface, which generally refers to the maximum fluctuation (fingering tip) in an experiment. Just above the transition, e.g., when $v_L = 1$ mm/s and $b_0 = 0.5$ mm, the maximum of $\Gamma(t)$, $\Gamma_{\max} = 1.02$, and the minimum of $\kappa^*(t)$, $\kappa^*(t)_{\min} = -5.47$. In this case, the perturbation growth toward the liquid interior exceeds the original interfacial curvature of
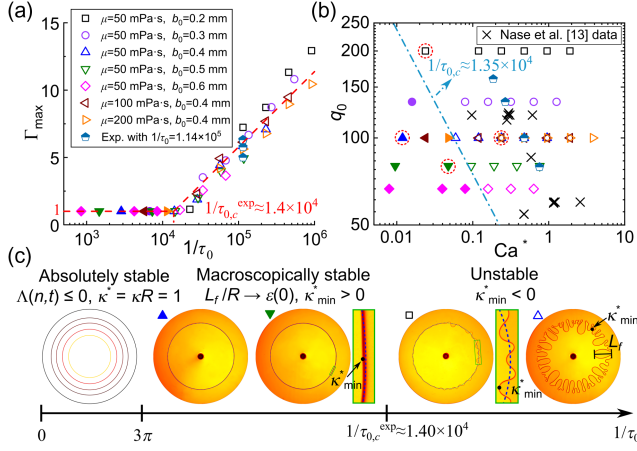
FIG. 2. (a) Maximum of normalized interfacial perimeter $\Gamma_{\max}$ as a function of $1/\tau_0$. (b) Phase diagram of interface stability in the space of capillary number Ca^* and aspect ratio q_0. The filled and open symbols denote the stable and unstable patterns, respectively, and the corresponding experimental images are listed in Fig. S2 [37]. Experimental data from Ref. [13] are also included. The blue dashed line represents the theoretical prediction $1/\tau_{0,c} = 1.35 \times 10^4$ through Eq. (4), separating the stable from the unstable regime. (c) Interfacial morphologies at different values of $1/\tau_0$. The image for $1/\tau_0 < 3\pi$ is obtained by numerically computed interface evolution. The other images represent the experimental cases circled in (b).

the system, and the interface manifests itself as an unstable morphology. Additionally, statistical results of $\kappa^*(t)_{\min}$ are summarized in Fig. S3 [37], which shows that $\kappa^*(t)_{\min}$ is less than zero in the unstable patterns. Thus, the condition of $\kappa^*(t)_{\min} = 0$ reasonably well divides the patterns in terms of stability.

Previous studies have shown that a modified capillary number $1/\tau_0$ is an important parameter governing fingering characteristics [28,29]; $1/\tau_0 = 12\mu v_L R_0^3/\sigma b_0^3$, proportional to the product of the capillary number $\mathrm{Ca}^* = \mu v_r/\sigma$ and the square of aspect ratio $q_0 = R_0/b_0$ with $v_r = v_L R_0/2b_0$ being the radial velocity of equivalent interface. Here, we show that $1/\tau_0$ also controls the stability transition, as characterized by the maximum perimeter length $\Gamma_{\max}$, which is a global measure of interface morphology. As shown in Fig. 2(a), $\Gamma_{\max}$ stays close to 1 until $1/\tau_0$ reaches a critical value $1/\tau_{0,c}^{\exp} = 1.40 \times 10^4$, beyond which $\Gamma_{\max}$ starts to rise sharply. We further plot all experimental observations in a phase diagram in the parameter space of Ca^* and q_0 [Fig. 2(b)], where the theoretical prediction, close to $1/\tau_{0,c}^{\exp}$, indeed separates the two regimes. It is worth pointing out that previous experimental studies [12,13,28,29] explored only the unstable regime. Additionally, cavitation as studied in Refs. [38–41] was not observed in our experiments.

We adopt the linear stability theory based on the gap-averaged flow equations to probe the interface evolution and instability mechanism. The perturbed interface evolves

in the linear regime by an azimuthal Fourier mode with wave number n: $\mathcal{R}(\theta, t') = R(t')[1 + \sum \zeta_n^*(t') \exp(in\theta)]$, where $t' = v_L t/b_0 = b/b_0 - 1$ is the dimensionless time; the individual dimensionless perturbation amplitudes $\zeta_n^*(t')$ and the corresponding growth rate $\Lambda(n, t')$ are calculated as [37]

$$\zeta_n^*(t') = \frac{\zeta_n(0)}{R(t')} \exp\left[\int_0^{t'} \Lambda(n, t') \mathrm{d}t'\right], \quad (1)$$

$$\Lambda(n, t') = \frac{1}{s(n, t')}\left\{\frac{1}{2(1 + t')}[|n| - s(n, t')]\right.$$
$$\left. - \frac{\pi}{4}\tau_0(1 + t')^{7/2}|n|(n^2 - 1)\right\}, \quad (2)$$

respectively, where $\zeta_n(0)$ is the initial interfacial (noise) amplitude at $t' = 0$; $s(n, t')$ is associated with the contribution of the viscous normal stress arising from radial velocity gradients [29,36], $s(n, t') = 1 + \delta(1 + t')^3(n^2 - |n|)/6q_0^2$, and $\delta = 1$ ($\delta = 0$) when the normal stress is (not) considered.

We further examine the criterion to predict the onset of interface instability. Equation (2) indicates that Λ decreases with t'. The finger decay stage of the unstable patterns at the later time proves this point, because the fluid viscous stress decays fast: $f_{\mathrm{vis}} \sim 12\mu v_r R/b^2 = 6\mu v_L R_0^2 b_0/(b_0 + v_L t)^4$. Thus, the maximum of the perturbation growth rate occurs at $t' = 0$; i.e., one needs only to check if $\Lambda(n, 0) < 0$, which results in the absolute stability threshold $1/\tau_{0,c} = 3\pi$ [42]. We confirm by numerical computation that the interface is indeed stable for $1/\tau_{0,c} < 3\pi$ [Fig. 2(c)]. Surprisingly, this threshold is several orders of magnitude smaller than the experimentally observed $1/\tau_{0,c}^{\exp}$. The onset of fingering occurs at much larger values of $1/\tau_0$ [Fig. 2(c)]; for example, even when $1/\tau_0 = 7.31 \times 10^3$ ($v_L = 0.5$ mm/s and $b_0 = 0.5$ mm) with positive $\Lambda(n, 0)$, the interface maintains macroscopically smooth at all times without apparent fingers.

This remarkably large discrepancy suggests that the growth rate-based stability criterion fails to predict the pattern transition. To reconcile this issue, we employ the linear stability theory to probe the spatiotemporal dynamics of growth rate and amplitude of perturbation. We compute the interface evolution with an initial perturbation which has a random noise amplitude $\zeta_n(0)$ and an n-dependent random phase angle [29,43]. $\zeta_n(0)$ can be reasonably assumed to obey an exponential distribution: $\zeta_n(0) = k_\zeta R_0 \exp(-a_\zeta n)$, where k_ζ is a coefficient mainly controlled by the cell roughness and a_ζ is a wave number coefficient reflecting the response of perturbations with different wave numbers. By comparing with experimental results of interfacial patterns and finger growth statistics, we set $k_\zeta = 1.9 \times 10^{-4}$ and $a_\zeta = 0.1$, which are justified by the experimental conditions (more details and parameter
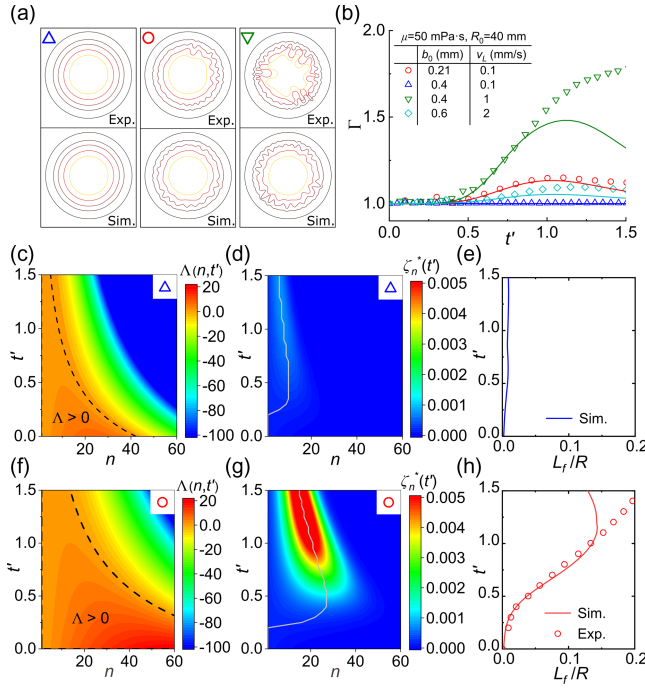
FIG. 3. (a) Comparison of interfacial evolution (the lines corresponding to times at $t' = 0$, 0.5, 1, 2, and 4) between experimental observations and theoretical calculations. The symbols represent the experimental conditions listed in (b). (b) Evolution of interfacial perimeter length Γ in representative experiments and simulations. (c)–(e) Maps of perturbation growth rate $\Lambda(n, t')$ and perturbation amplitude $\zeta_n^*(t')$ and evolution of normalized maximum finger length L_f/R for $v_L = 1$ mm/s and $b_0 = 0.4$ mm. (f)–(h) The same as (c)–(e) but for $v_L = 0.1$ mm/s and $b_0 = 0.21$ mm. The dashed lines in (c) and (f) denote $\Lambda = 0$, and the gray lines in (d) and (g) represent the maximum of $\zeta_n^*(t')$.

sensitivity analysis in [37]). Figures 3(a) and 3(b) show that the simulated interfacial shapes and perimeter lengths are consistent with the experimental observations for the macroscopically stable and the fingering patterns. Thus, the linear stability theory is effective in calculation of the growth and amplitude of perturbation, especially at the early stage. At the later stage with highly developed fingering patterns, the predicted interfacial morphologies deviate slightly from that of the experiments.

We further show the growth and amplitude of perturbation for the macroscopically stable case in Figs. 3(c)–3(e) and for an unstable case in Figs. 3(f)–3(h), which is solved by using Eqs. (1) and (2). The growth rate of perturbation $\Lambda(n, t')$ for a small wave number decreases from positive values to negative values with time t', which causes the perturbation amplitude $\zeta_n^*(t')$ to increase first and then decrease. The variation of perturbation amplitude is consistent with the experimental observation of the growth and decay of fingering [Fig. 1(b)]. Additionally, comparison between Figs. 3(c) and 3(f) shows that the perturbations of the unstable case have larger growth rates with a longer

positive duration than the macroscopically stable case. Thus, perturbations of large amplitude for a broad range of wave numbers exist in the unstable case, resulting in large observable fingers. The simulated maximum finger length normalized by the equivalent radius, L_f/R, is consistent with the experiments [Figs. 3(e) and 3(h)]. The inward-growing fingers of air leads to negative local interfacial curvature at the fingering tip. Hence, one can link the occurrence of instability to the condition of minimum local in-plane curvature along the interface being equal to 0. To simplify the derivation of the criterion, here we consider the contribution of the maximum amplitude component (with wave number N) of perturbation to the minimum local in-plane curvature and establish a new perturbation amplitude-based criterion according to the curvature formula $\kappa^* = 1 - \zeta^* - \partial^2 \zeta^*/\partial\theta^2$ normalized by $1/R$ [1]:

$$\kappa_{\min}^*(\zeta_N^*) = \min_\theta \left\{ 1 - \zeta_N^* e^{iN\theta} - \zeta_N^* \frac{\partial^2 e^{iN\theta}}{\partial\theta^2} \right\} = 0. \quad (3)$$

The minimum value $\kappa_{\min}^*(\zeta_N^*)$ corresponds to the condition $\exp(iN\theta) = -1$, and Eq. (3) can be simplified as $(N^2 - 1)\zeta_N^* = 1$, where N is the wave number of maximum perturbation amplitude component, e.g., gray lines in Figs. 3(d) and 3(g). When ignoring the viscous normal stress ($\delta = 0$), substituting Eqs. (1) and (2) into $(N^2 - 1)\zeta_N^* = 1$ can give a semianalytical equation, from which the critical value $1/\tau_{0,c}$ can be solved:

$$(N^2 - 1)k_\zeta(1 + t_c')^{1/2} \exp\left[-a_\zeta N + \frac{\ln(1 + t_c')}{2}(N - 1) \right.$$
$$\left. - \frac{\pi}{18}\tau_{0,c}[(1 + t_c')^{9/2} - 1](N^3 - N) \right] = 1, \quad (4)$$

where t_c' is the time satisfying $d[(N^2 - 1)\zeta_N^*]/dt' = 0$ [37]. Building upon the wavelength selection by maximizing the amplitude $[\partial\zeta_n^*(t')/\partial n = 0]$ in previous work [29] and further simplifying for the condition $\delta = 0$, we derive a simplified analytical equation to determine the maximum-amplitude wave number N:

$$N = \sqrt{\frac{1}{3}\left(1 + \frac{9[\ln(1 + t') - 2a_\zeta]}{\pi\tau_0[(1 + t')^{9/2} - 1]} \right)}. \quad (5)$$

By substituting Eq. (5) into Eq. (4), one can iteratively solve the set of equations to obtain a critical value of $1/\tau_{0,c} = 1.35 \times 10^4$, which closely matches the experimental threshold $1/\tau_{0,c}^{\exp} = 1.40 \times 10^4$. This excellent agreement further confirms the validity of the new criterion based on perturbation amplitude.

Focusing on the fingering morphology, we further probe the hierarchical structure and evolution of the interfacial
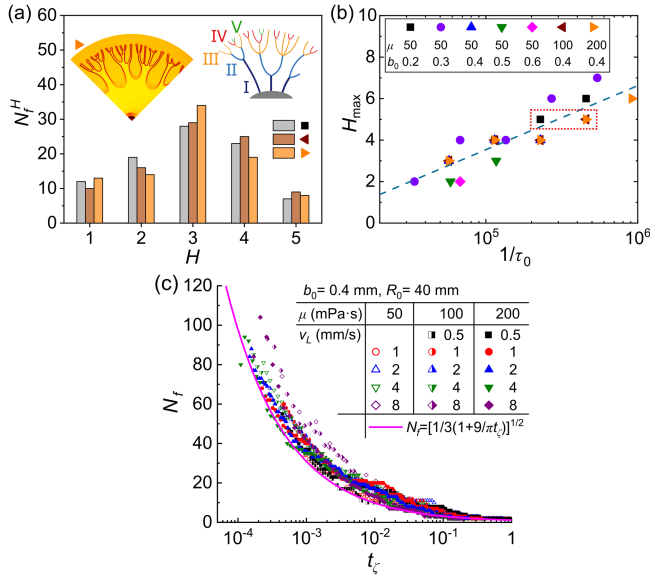
FIG. 4. (a) Finger number N_f for each hierarchical level H for three cases. The insets show a representative image and the corresponding schematic of hierarchy. (b) Variation of the maximum number of hierarchical levels H_{max} with $1/\tau_0$. (c) Data collapse of N_f with the dimensionless characteristic time t_ζ. The pink line represents theoretical prediction.

patterns. The hierarchical structure originates from the competition during the growth of multiple fingers. Limited by the geometric space, few fingers continue to grow and eventually develop into dominant fingers, which inhibits the growth of adjacent fingers and gives rise to a dendritic liquid structure [insets in Fig. 4(a)]. We examine the relationship between the hierarchical levels of the structure and the corresponding number of fingers when the number of hierarchical levels H reaches the maximum in each experiment. Interestingly, the number of fingers N_f^H is largest at the intermediate hierarchy levels for the highly developed fingering patterns [Fig. 4(a)]. This can be explained by the combined effects of space restriction (which means only a few dominant fingers are allowed at low order and, thus, set an upper limit of finger size) and capillary smoothening (which sets a lower limit). Furthermore, for the unstable cases, the maximum order number H_{max} increases roughly linearly with $\log(1/\tau_0)$ [Fig. 4(b)], indicating that the interface evolution is indeed controlled by the parameter $1/\tau_0$.

The derived analytical expression for the maximum-amplitude wave number N is also used to predict the finger number N_f. According to Eq. (5), a dimensionless characteristic time can be defined as $t_\zeta = \tau_0[(1+t')^{9/2} - 1]/[\ln(1+t') - 2a_\zeta]$, and $N_f = [1/3(1 + 9/\pi t_\zeta)]^{1/2}$. Figure 4(c) shows that the variations of N_f with t_ζ for all experiments well collapse and are well predicted. Note that the viscous normal stress, arising from radial velocity gradients, is ignored in order to derive the analytical expressions [Eqs. (4) and (5)]. Nevertheless, the solutions demonstrate sufficient accuracy for predicting the onset of instability and number of fingers. The relative impact of normal stress is further discussed in [37]. Additionally, this work does not consider the rheological effects due to interface laden with surfactants, particles, proteins, etc., which may contribute to enhancing interfacial destabilization [31].

In summary, we present a systematic study of the interfacial stability in gap expansion-driven flow. Surprisingly, we discover that macroscopically stable interfaces, previously considered unattainable practically, can be obtained for a wide range of initial gaps and gap expansion rates. We demonstrate that a modified capillary number $1/\tau_0$ governs the stability transition. The perturbation growth rate-based criterion fails to predict the experimentally observed transition from stable to unstable patterns, which occurs at the threshold $1/\tau_0 = 1.40 \times 10^4$. We propose a new criterion based on perturbation amplitude and minimum in-plane curvature to predict the onset of instability, which is in excellent agreement with the experimental results. We further show that the fingering pattern evolves to yield a hierarchical liquid structure and derive a new, simple analytical expression which captures the evolution characteristics of fingering. These results pave the way for controlling interfacial stability and fingering morphology evolution, which are significant in a plethora of natural processes and industrial applications. For instance, the established threshold of stability can provide us with suitable parametric combinations of fluid properties and expansion rates for achieving interface stability while impeding fingering growth, which can be tailored, e.g., to optimize adhesive performance and to improve flow efficiencies in hydrofractures for oil and gas recovery. Additionally, the formation and characteristics of dendritic fingering structures may shed light on the hierarchical branching process of bronchial tree [13] and alveolar epithelial cell differentiation during lung development [44]. Furthermore, this work can also provide critical insights for the applications of amplitude-based criterion in other flow configurations, e.g., by adjusting the perturbation amplitude equations (1) and (2) to derive the matching criterion. Further investigations need to address the impacts of fluid rheology, interfacial tension, wettability, surface roughness, and geometrical configuration.

*Contact author: zbyang@whu.edu.cn
†Contact author: csyfchen@whu.edu.cn

[1] L. Paterson, Radial fingering in a Hele Shaw cell, J. Fluid Mech. **113**, 513 (1981).

[2] S. Li, J. S. Lowengrub, J. Fontana, and P. Palffy-Muhoray, Control of viscous fingering patterns in a radial Hele-Shaw cell, Phys. Rev. Lett. **102**, 174501 (2009).

[3] B. Sandnes, E. Flekkøy, H. Knudsen, K. Måløy, and H. See, Patterns and flow in frictional fluid dynamics, Nat. Commun. **2**, 288 (2011).

[4] B. Levaché and D. Bartolo, Revisiting the Saffman-Taylor experiment: Imbibition patterns and liquid-entrainment transitions, Phys. Rev. Lett. **113**, 044501 (2014).

[5] J. Kim, F. Xu, and S. Lee, Formation and destabilization of the particle band on the fluid-fluid interface, Phys. Rev. Lett. **118**, 074501 (2017).

[6] E. Ben-Jacob, From snowflake formation to growth of bacterial colonies II: Cooperative formation of complex colonial patterns, Contemp. Phys. **38**, 205 (1997).

[7] S. Mark, R. Shlomovitz, N. S. Gov, M. Poujade, E. Grasland-Mongrain, and P. Silberzan, Physical model of the dynamic instability in an expanding cell culture, Biophys. J. **98**, 361 (2010).

[8] M. Heil and A. L. Hazel, Fluid-structure interaction in internal physiological flows, Annu. Rev. Fluid Mech. **43**, 141 (2011).

[9] A. Heap and A. Juel, Anomalous bubble propagation in elastic tubes, Phys. Fluids **20**, 081702 (2008).

[10] R. W. Edwards, F. Doster, M. A. Celia, and K. W. Bandilla, Numerical modeling of gas and water flow in shale gas formations with a focus on the fate of hydraulic fracturing fluid, Environ. Sci. Technol. **51**, 13779 (2017).

[11] Z. Yang, Y. Méheust, I. Neuweiler, R. Hu, A. Niemi, and Y.-F. Chen, Modeling immiscible two-phase flow in rough fractures from capillary to viscous fingering, Water Resour. Res. **55**, 2033 (2019).

[12] A. Lindner, D. Derks, and M. Shelley, Stretch flow of thin layers of Newtonian liquids: Fingering patterns and lifting forces, Phys. Fluids **17**, 072107 (2005).

[13] J. Nase, D. Derks, and A. Lindner, Dynamic evolution of fingering patterns in a lifted Hele-Shaw cell, Phys. Fluids **23**, 123101 (2011).

[14] T. T. Al-Housseiny, P. A. Tsai, and H. A. Stone, Control of interfacial instabilities using flow geometry, Nat. Phys. **8**, 747 (2012).

[15] G. Bongrand and P. A. Tsai, Manipulation of viscous fingering in a radially tapered cell geometry, Phys. Rev. E **97**, 061101(R) (2018).

[16] L. C. Morrow, T. J. Moroney, and S. W. McCue, Numerical investigation of controlling interfacial instabilities in nonstandard Hele-Shaw configurations, J. Fluid Mech. **877**, 1063 (2019).

[17] D. Pihler-Puzović, P. Illien, M. Heil, and A. Juel, Suppression of complex fingerlike patterns at the interface between air and a viscous fluid by elastic membranes, Phys. Rev. Lett. **108**, 074502 (2012).

[18] B. Saintyves, O. Dauchot, and E. Bouchaud, Bulk elastic fingering instability in Hele-Shaw cells, Phys. Rev. Lett. **111**, 047801 (2013).

[19] D. Pihler-Puzović, G. G. Peng, J. R. Lister, M. Heil, and A. Juel, Viscous fingering in a radial elastic-walled Hele-Shaw cell, J. Fluid Mech. **849**, 163 (2018).

[20] R. Arun, S. T. M. Dawson, P. J. Schmid, A. Laskari, and B. J. McKeon, Control of instability by injection rate oscillations in a radial Hele-Shaw cell, Phys. Rev. Fluids **5**, 123902 (2020).

[21] Í. M. Coutinho and J. A. Miranda, Control of viscous fingering through variable injection rates and time-dependent viscosity fluids: Beyond the linear regime, Phys. Rev. E **102**, 063102 (2020).

[22] E. O. Dias, E. Alvarez-Lacalle, M. S. Carvalho, and J. A. Miranda, Minimization of viscous fluid fingering: A variational scheme for optimal flow rates, Phys. Rev. Lett. **109**, 144502 (2012).

[23] Z. Zheng, H. Kim, and H. A. Stone, Controlling viscous fingering using time-dependent strategies, Phys. Rev. Lett. **115**, 174501 (2015).

[24] P. H. A. Anjos, E. O. Dias, L. Dias, and J. A. Miranda, Adhesion force in fluids: Effects of fingering, wetting, and viscous normal stresses, Phys. Rev. E **91**, 013003 (2015).

[25] K. R. Shull, C. M. Flanigan, and A. J. Crosby, Fingering instabilities of confined elastic layers in tension, Phys. Rev. Lett. **84**, 3057 (2000).

[26] D. Derks, A. Lindner, C. Creton, and D. Bonn, Cohesive failure of thin layers of soft model adhesives under tension, J. Appl. Phys. **93**, 1557 (2003).

[27] Q. Barral, G. Ovarlez, X. Chateau, J. Boujlel, B. Rabideau, and P. Coussot, Adhesion of yield stress fluids, Soft Matter **6**, 1343 (2010).

[28] M. J. Shelley, F.-R. Tian, and K. Wlodarski, Hele-Shaw flow and pattern formation in a time-dependent gap, Nonlinearity **10**, 1471 (1997).

[29] E. O. Dias and J. A. Miranda, Determining the number of fingers in the lifting Hele-Shaw problem, Phys. Rev. E **88**, 043002 (2013).

[30] S. D. Kanhurkar, V. Patankar, T. Ul Islam, P. S. Gandhi, and A. Bhattacharya, Stability of viscous fingering in lifted Hele-Shaw cells with a hole, Phys. Rev. Fluids **4**, 094003 (2019).

[31] Í. M. Coutinho and J. A. Miranda, Role of interfacial rheology on fingering instabilities in lifting Hele-Shaw flows, Phys. Rev. E **108**, 025104 (2023).

[32] J. Bohr, S. Brunak, and T. Nørretranders, Viscous trees and voronoi-structure formation in expanding systems, Europhys. Lett. **25**, 245 (1994).

[33] J. Nase, A. Lindner, and C. Creton, Pattern formation during deformation of a confined viscoelastic layer: From a viscous liquid to a soft elastic solid, Phys. Rev. Lett. **101**, 074503 (2008).

[34] Y. M. Abdelhaye, M. Chaouche, and H. Van Damme, The tackiness of smectite muds. 1. The dilute regime, Appl. Clay Sci. **42**, 163 (2008).

[35] T. Divoux, A. Shukla, B. Marsit, Y. Kaloga, and I. Bischofberger, Criterion for fingering instabilities in colloidal gels, Phys. Rev. Lett. **124**, 248006 (2020).

[36] E. O. Dias and J. A. Miranda, Wavelength selection in Hele-Shaw flows: A maximum-amplitude criterion, Phys. Rev. E **88**, 013016 (2013).

[37] See Supplemental Material at http://link.aps.org/supplemental/10.1103/PhysRevLett.133.034003 for Figs. S1–S3, Table S1, experimental procedure, and theoretical derivation.

[38] A. J. Crosby, K. R. Shull, H. Lakrout, and C. Creton, Deformation and failure modes of adhesively bonded elastic layers, J. Appl. Phys. **88,** 2956 (2000).

[39] S. Poivet, F. Nallet, C. Gay, and P. Fabre, Cavitation-induced force transition in confined viscous liquids under traction, Europhys. Lett. **62,** 244 (2003).

[40] Y. Mohamed Abdelhaye, M. Chaouche, J. Chapuis, E. Charlaix, J. Hinch, S. Roux, and H. Van Damme, Tackiness and cohesive failure of granular pastes: Mechanistic aspects, Eur. Phys. J. E **35,** 45 (2012).

[41] S. Lin, Y. Mao, R. Radovitzky, and X. Zhao, Instabilities in confined elastic layers under tension: Fringe, fingering and cavitation, J. Mech. Phys. Solids **106,** 229 (2017).

[42] When ignoring the effects of normal stress, it can be obtained from Eq. (2) that $\Lambda(n, 0) < 0$ gives the critical condition $n_c > [2/(\pi\tau_{0,c}) + 1/4]^{1/2} - 1/2$ [30]. If $n_c < 2$, all perturbations will be suppressed [23,30], thus resulting in the absolute stability threshold $1/\tau_{0,c} = 3\pi$.

[43] J. Miranda and M. Widom, Radial fingering in a Hele-Shaw cell: A weakly nonlinear analysis, Physica D (Amsterdam) **120,** 315 (1998).

[44] J. Li, Z. Wang, Q. Chu, K. Jiang, J. Li, and N. Tang, The strength of mechanical forces determines the differentiation of alveolar epithelial cells, Dev. Cell **44,** 297 (2018).